Computers and Concrete, *Vol. 16, No. 4 (2015) 643-667*
DOI: http://dx.doi.org/10.12989/cac.2015.16.4.643

Simulation study on dynamic response of precast frames made of recycled aggregate concrete

ThiLoan Pham[1,2], Jianzhuang Xiao[*1] and Tao Ding[1]

[1]*Department of Structural Engineering, Tongji University, Shanghai, 200092, PR China*
[2]*Department of Civil Engineering, Haiphong University, Haiphong, 180000, Vietnam*

(Received May 22, 2015, Revised July 10, 2015, Accepted October 28, 2015)

Abstract. 3-dimentional precast recycled aggregate concrete (RAC) finite element models were developed by means of the platform OpenSees to implement sophisticated nonlinear model subjected to seismic loads. Efforts were devoted to the dynamic responses (including dynamic characteristics, acceleration amplifications, displacements, story drifts) and capacity curve. In addition, this study extended the prediction on dynamic response of precast RAC model by parametric study of material properties that represent the replacement percentage of recycled coarse aggregate (RCA). Principles and assumptions that represent characteristics of precast structure and influence of the interface between head of column and cast-in-place (CIP) joint on the stiffness of the joints was put forward and validated by test results. The comparison between simulated and tested results of the precast RAC frame shows a good correlation with most of the relative errors about 25% in general. Therefore, the adopted assumptions and the platform OpenSees are a viable approach to simulate the dynamic response of precast frames made of RAC.

Keywords: recycled aggregate concrete (RAC); precast frame; dynamic responses; dynamic nonlinear analysis; simulated result; tested result; interface

1. Introduction

As recycled aggregated concrete (RAC) has widely been recognized as a structural material, studies on mechanical properties have become a focal topic in the current literature. These studies have, to some extent, contributed to understanding the characteristics and behaviors of RAC such as mixture ratio, strength, elastic modulus, stress-strain relationship, and durability. More specifically, these studies have indicated some noticeable conclusions. Studies on fundamental behaviors of RAC have been investigated comprehensively (Limbachiya 2004, Lo 2008, Bhikshma and Kishore 2010, Fonseca *et al*. 2011, Xiao *et al*. 2012). For instance, the compressive, tensile and shear strengths of RAC are generally lower than those of natural aggregate concrete (NAC); the modulus of elasticity for RAC generally reduces as the recycled coarse aggregate (RCA) replacement percentage increases; the RCA replacement percentage has only nominal influence on the bond strength between RAC and deformed rebars. Added to these, studies on the

∗Corresponding author, Professor, E-mail: jzx@tongji.edu.cn

http://www.techno-press.org/?journal=cac&subpage=8 ISSN: 1598-8198 (Print), 1598-818X (Online)

structural performance of RAC have also been investigated not only on elements but also on structures subjected to both static and dynamic loads. For instance, studies on beams (Fathifazl *et al.* 2009, 2010, Xiao *et al.* 2014a), columns (Xiao *et al.* 2012), beam-column joints(Xiao *et al.* 2010), slabs (Xiao *et al.* 2015b) and frames (Xiao *et al.* 2006, Cao *et al.* 2011). The positive results of these studies further support and strengthen the possibilities of applying RAC in civil engineering structures. Especially, the seismic performance of both components and structures of RAC have been performed in recent years by some researchers (Du and Wang 2015, Xiao *et al.* 2012, Zhang *et al*. 2012). However, the current literature on RAC reveals that most of the studies focus on monolithic (wholly cast-in-situ) structures and the topics of earthquake response of precast RAC structures seem to be ignored. In addition, the properties of RAC are influenced greatly by preparation condition of mix proportion (Parekh and Modhera 2011), and it is well known that mixing concrete will be controlled much better in factory conditions. Therefore, the authors suggest that RAC components can be produced in precast factories in order to take inherent advantages of precast elements and ensure the quality of construction. From the view of combination between RAC and prefabrication, the precast RAC components are feasible to use and develop application of RAC in civil engineering as a structural material. Therefore, the overall structural response of a space precast frame made of RAC subjected to seismic loads was carried out by shaking table test and investigated by authors in order to validate simulated results of a 3-dimentional precast RAC finite element model.

Static and dynamic nonlinear analysis of reinforced concrete structures have been researched for decades. It can be clearly seen that dynamic nonlinear analysis of the inelastic responses of structures subjected to dynamic loads such as seismic load is one of the most difficult tasks. There have been many dynamic nonlinear analyses carried out to predict the dynamic response (D'Amato *et al*. 2012, Quaranta *et al*. 2012, Xiao *et al*. 2014b) since a number of computer programs have been developed for nonlinear finite element analysis of reinforced concrete structures such as Ansys, Abquas, SAP 2000, OpenSees and so on. Among these programs, the Open System for Earthquake Engineering Simulation (OpenSees) is one of the prominent software for simulating dynamic responses of structural systems. As a result, OpenSees has been employed in many researches on the overall structural dynamic response of both reinforced concrete and steel structures (Gavali and Shah 2008, Morales 2011, Xiao *et al*. 2014b) and experimental results verified a capable prediction of structural response subjected to strong earthquake excitations. Therefore, this study aims at comprehensive understanding of the dynamic response of 3-dimensional RAC precast frames by developing sophisticated nonlinear finite element models by OpenSees. The dynamic responses including dynamic characteristics, acceleration amplifications, displacements, story drifts and capacity curve were analyzed and compared to those obtained from shaking table test. In addition, parametric study of material properties was also conducted through the replacement percentage of Recycled Coarse Aggregate (RCA). Moreover, the interface effect between head of columns and cast-in-place (CIP) joint was comprehensively analyzed and evaluated through both simulation and comparison with characteristic of a similar CIP frame structures made of RAC.

2. Research significance

Some 3-dimentional precast RAC finite element models were developed to implement sophisticated nonlinear model in the numerical simulation analysis in order to reproduce the

dynamic response observed by shaking table test and extend the prediction on dynamic response of precast RAC model by parametric study of material properties. Based on the achievements inferred from simulated results, the influence of interface between head of columns and CIP joint was revealed. The results of this study will contribute to the view of combination between RAC and prefabrication both theoretical field and practice design/construction.

3. General introduction on the precast RAC model and shaking table test.

3.1 Description of the model

The tested model was designed by scaling down the geometric from prototype structure and the dimension scaling parameter was taken as 1:4 due to the limitation of shake-table parameters of the State Key Laboratory for Disaster Reduction in Civil Engineering at Tongji University. The main similarity relations between the prototype structure and the model, the diameter range of recycled coarse aggregate (RCA), the proportion of recycled concrete mixture of nominal strength grade C30 and the measured average mechanical properties of the fine iron wires can be found in detail from Xiao *et al.* (2015a).

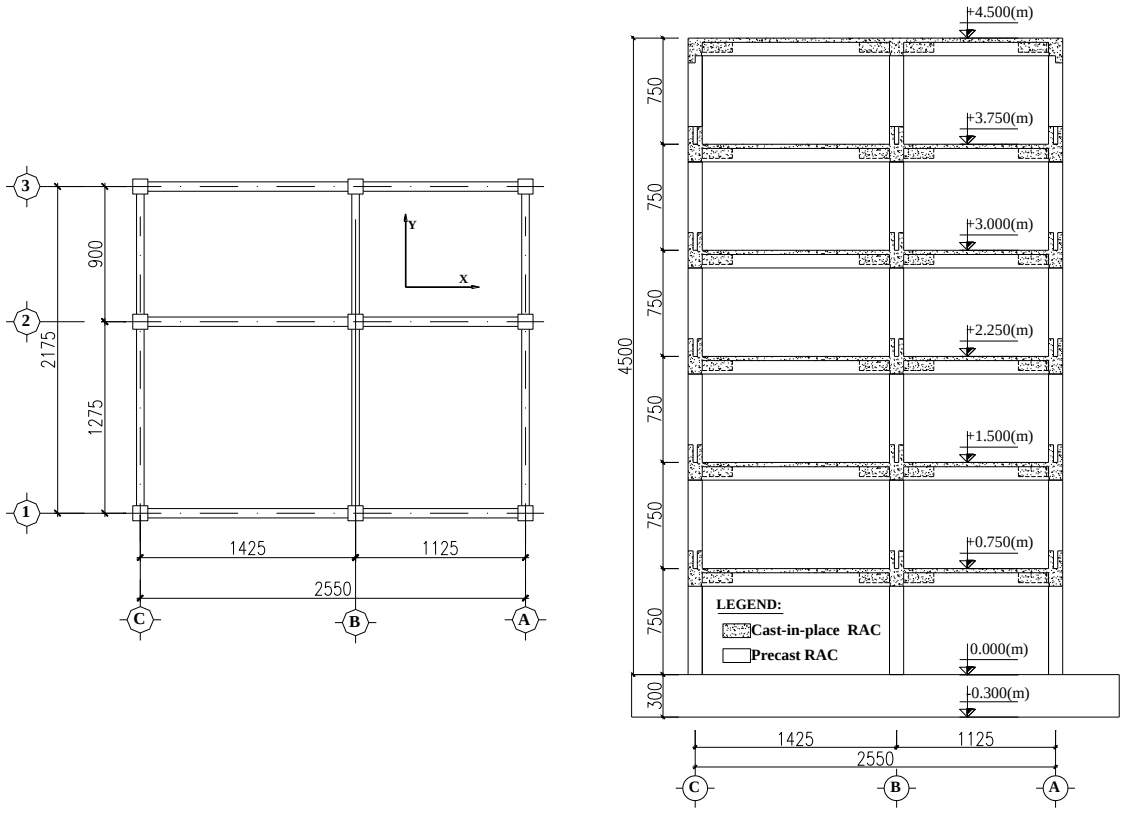

(a) Plan view (b) Elevation view

Fig. 1 Configuration and reinforcement of the model (Unit: mm)

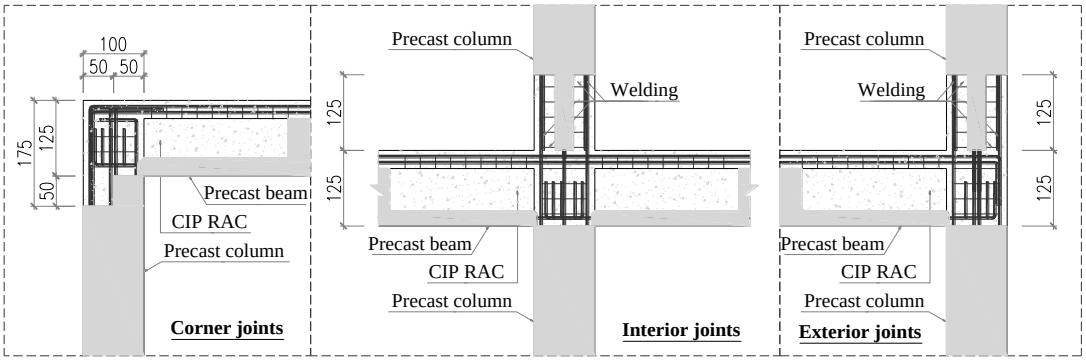

(a) Corner joint (b) Interior joint (c) Exterior joint

Fig. 2 Joint detail of precast frame

The tested model was a two-bay, two-span and six-story frame structure regular in elevation. The RAC frame model was 2175×2550mm in plan and had a constant story height of 750mm as presented in Fig. 1. Column, beam sections and the details of the reinforcing bar in the columns, beams as well as beam-column joints are presented in Xiao *et al*. (2015a). Fig. 2 describes three typical joints of the precast RAC model.

In order to measure the acceleration, a total of 30 accelerometers were installed, with 2 on the ground floor on both the *X* and *Y*-directions, 4 on each floor from the 1st to the 5th floor, and 8 on the roof. In order to measure the displacement, a total of 14 displacement Linear Variable Differential Transducers (LVDTs) were installed, with 2 on each floor from the 1st to the 5th in both *X* and *Y*-directions, and 4 on the roof.

3.2 Seismic waves and loading program

According to the *Code for seismic design of buildings* (Chinese standard GB 50011-2010), Wenchuan seismic wave (WCW, 2008, N-S) should be considered for Type-II site soil in term of acceleration spectra as described in Fig. 3(a). Considering the spectral density properties of Type-II site soil as shown in Fig. 3(b), El Centro wave (ELW, 1940, N-S) was also selected. Shanghai artificial wave (SHW) were also used for comparison analysis purpose as shown in Fig. 3(c).

The loading program consisted of 8 levels for peak ground acceleration (PGA) and the detail of loading program is presented in Table 1.

4. Simulation modeling

4.1 Principles and assumptions

The factors necessary to be taken into considerations in modeling precast frame made of RAC are, (1) the difference of precast concrete section from cast-in-place concrete section, including the location of longitudinal bar, cover concrete thickness, (2) the difference in compressive strength of concrete for cast-in-place concrete and precast concrete, (3) the interface between head of column and CIP joint which causes reduction of strength and stiffness of the joint where the lower column

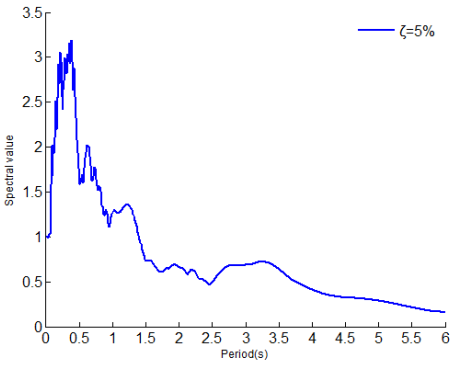

(a) Acceleration spectra of WCW

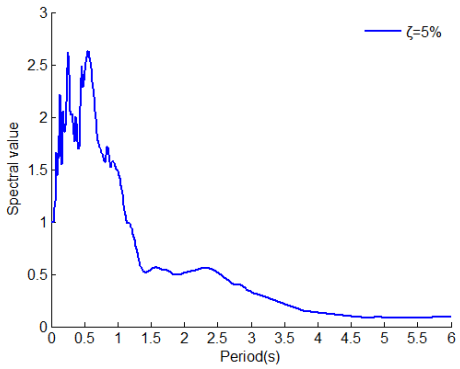

(b) Acceleration spectra of ELW

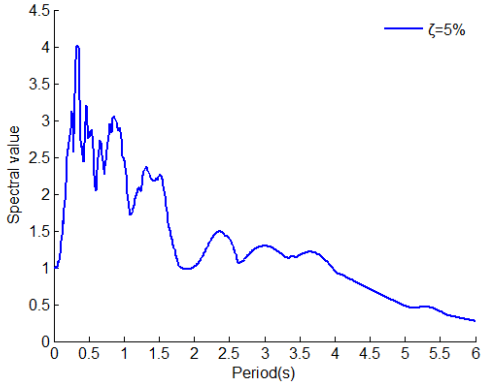

(c) Acceleration spectraof SHW

Fig. 3 Earthquake input motions

framing into due to the reduced contribution of the moment resistance of the lower column, and (4) constitutive model for concrete with recycled coarse aggregates.

The considerations (1) and (2) were governed well by modeling sections of precast beam and column elements precisely as sections designed. The third consideration, thanks to the assumption of rigid joint which is presented by rigid end zones in the beams and columns framing into the joint, the head and foot column sections were modeled.

The head cross sections of columns were reduced 30% compared with middle section of columns in order to reflect the interface behavior between precast columns and CIP joints. The foot cross section of columns were increase 20% in order to take the contribution of monolithic structural parts including foot of column, beam and slab, to stiffness of joints.

The cross sections of head and foot columns were calibrated with the following rules:

(1) The initial natural frequency must be close to initial natural frequencies obtained from test result.

(2) Mode shape coefficients of the first vibration in both *X* and *Y*-direction must be close to those obtained from shaking table test.

The last consideration was highly respected by material parameters used in modeling concrete model such as compressive strength, modulus elastic.

Table 1 Loading program

No.	Input	PGA (g)			No.	Input	PGA (g)		
		X-direction					*X*-direction		
		Designed	Measured	Variation (%)			Designed	Measured	Variation (%)
1	White noise	0.050	0.032	-36.00	18	WCW	0.370	0.374	1.08
2	WCW	0.066	0.075	14.09	19	ELW	0.370	0.349	-5.68
3	ELW	0.066	0.067	1.21	20	SHW	0.370	0.278	-24.86
4	SHW	0.066	0.068	2.58	21	White noise	0.050	0.036	-28.00
5	White noise	0.050	0.037	-26.40	22	WCW	0.415	0.443	6.75
6	WCW	0.130	0.139	7.31	23	ELW	0.415	0.440	6.02
7	ELW	0.130	0.135	3.85	24	SHW	0.415	0.438	5.54
8	SHW	0.130	0.146	12.00	25	White noise	0.050	0.034	-31.20
9	White noise	0.050	0.037	-26.00	26	WCW	0.550	0.595	8.18
10	WCW	0.185	0.231	24.86	27	ELW	0.550	0.548	-0.36
11	ELW	0.185	0.197	6.49	28	SHW	0.550	0.561	2.00
12	SHW	0.185	0.175	-5.41	29	White noise	0.050	0.035	-30.00
13	White noise	0.050	0.036	-28.00	30	WCW	0.750	0.744	-0.80
14	WCW	0.264	0.273	3.41	31	ELW	0.750	0.766	2.13
15	ELW	0.264	0.261	-1.14	32	White noise	0.050	0.036	-28.00
16	SHW	0.264	0.269	1.89	33	SHW	0.750	0.679	-9.47
17	White noise	0.050	0.035	-30.00	34	White noise	0.050	0.036	-28.00

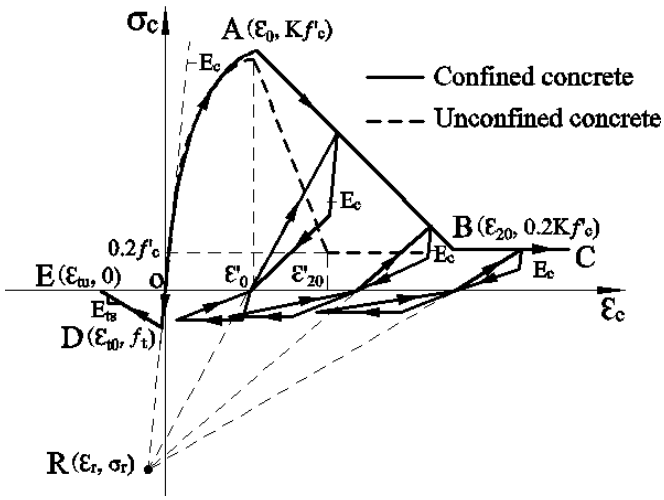

Fig. 4 Kent-Scott-Park model for concrete

4.2 Material properties and models

The monotonic envelope curve of the hysteretic model for concrete in compression follows the monotonic stress-strain relation model of Kent and Park (1971) as extended by Scott *et al.* (1982).

Even though more accurate and complete monotonic stress-strain models have been published before, the so-called modified Kent and Park model offers a good balance between simplicity and accuracy, and is widely used. Then the hysteretic unloading and reloading rules proposed by Yassin (Yassin 1994) are a set of linear stress-strain relations. Finally, in the numerical modeling of the RAC space frame, the hysteretic material model of concrete is illustrated in Fig. 4.

The concrete model takes into account the confinement effect due to the stirrups through modifying concrete strength parameters, because it is well known that the confined concrete by suitable arrangements of transverse reinforcement achieves a significant increase in both the strength and the ductility of compressed concrete (Mander *et al*. 1988, Montya 2000). The tensile behavior of the concrete model takes into account tension stiffening, and the degradation of the unloading and reloading stiffness for increasing values of the tensile strain after initial cracking. In this study, the maximum tensile strength f_t=0.07f'_c, and the tension stiffening modulus E_{ts}=0.05E_c (Orakca *et al*. 2006) were adopted. The other parameters of material properties used in modeling beams and columns as detailed in Tables 2-3.

The hysteretic material model used for the steel can reflect strain hardening and softening in the loading process, and takes into account pinching of force and deformation and unloading stiffness

Table 2 RAC material model parameters for beams

Index		Unconfined concrete Elastic modulus					Unconfined concrete Elastic modulus				
		f_c' (MPa)	ε_o' (10^{-3})	$0.2f_c'$ (MPa)	ε_{20}' (10^{-3})	E_c (GPa)	Kf_c' (MPa)	ε_o' (10^{-3})	$0.2Kf_c'$ (MPa)	ε_{20}' (10^{-3})	E_c (GPa)
		Precast RAC					**Cast-in-place RAC**				
Floor	1F	32.53	2.09	6.51	3.27	24.80	30.35	2.05	6.07	3.32	24.26
	2F	25.99	1.98	5.20	3.45	23.03	37.17	2.16	7.43	3.16	25.78
	3F	27.99	2.01	5.60	3.39	23.63	32.02	2.08	6.40	3.28	24.68
	4F	26.29	1.98	5.26	3.44	23.12	32.61	2.09	6.52	3.26	24.82
	5F	23.96	1.94	4.79	3.53	22.35	29.08	2.03	5.82	3.36	23.93
	6F	31.98	2.08	6.40	3.28	24.67	28.10	2.01	5.62	3.39	23.66

Table 3 RAC material model parameters for columns

Index		Unconfined concrete Elastic modulus					Confined concrete Elastic modulus				
		f_c' (MPa)	ε_o' (10^{-3})	$0.2f_c'$ (MPa)	ε_{20}' (10^{-3})	E_c (GPa)	Kf_c' (MPa)	ε_o' (10^{-3})	$0.2Kf_c'$ (MPa)	ε_{20}' (10^{-3})	E_c (GPa)
		Precast RAC					**Cast-in-place RAC**				
Floor	1F	27.842	2.000	5.568	4.634	23.58	35.87	2.577	7.175	53.369	23.58
	2F	26.315	2.000	5.263	4.841	23.13	34.35	2.611	6.869	53.556	23.13
	3F	29.009	2.000	5.802	4.495	23.91	37.04	2.554	7.408	53.244	23.91
	4F	28.882	2.000	5.776	4.510	23.88	36.91	2.556	7.383	53.257	23.88
	5F	28.309	2.000	5.662	4.577	23.72	36.34	2.568	7.268	53.317	23.72
	6F	27.718	2.000	5.544	4.650	23.55	35.75	2.580	7.150	53.383	23.55

Table 4 Longitudinal steel rebar material model parameters

Index		D (mm)	s_{1p} (MPa)	e_{1p}	s_{2p} (MPa)	e_{2p}	s_{3p} (MPa)	e_{3p}
Type	8#	3.94	329.36000	0.00165	431.79096	0.05117	230.55200	0.25000
	10#	3.32	281.52000	0.00175	411.15996	0.08248	287.81197	0.25000

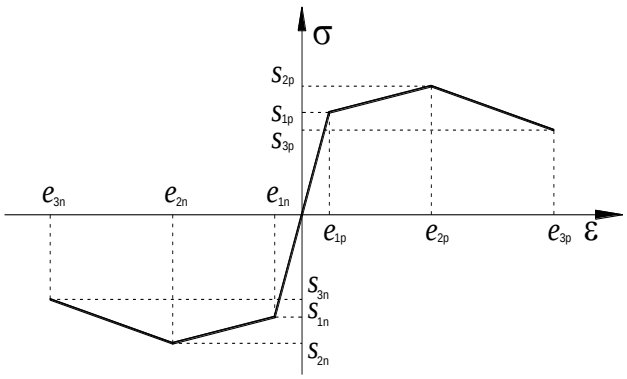

Fig. 5 Hysteretic material model for steel reinforcement

degradation based on the ductility, and involves a material damage model related to the material ductility and the energy dissipation. The material model (Mazzoni *et al*. 2011) for the steel bar was shown in Table 4 and Fig. 5. As shown in Fig. 5 (s_{1p}, e_{1p}), (s_{2p}, e_{2p}) and (s_{3p}, e_{3p}) represents stress and strain at yielding, maximum and ultimate point of the backbone curve in the positive direction, respectively, whereas (s_{1n}, e_{1n}), (s_{2n}, e_{2n}) and (s_{3n}, e_{3n}) represents stress and strain at yielding, maximum and ultimate point of the backbone curve in the negative direction, respectively.

4.3 Flexibility-based fiber elements

In order to accurately model the behavior of a reinforced concrete frame, the response of the beam and column cross sections must be captured. The fiber section model (Taucer *et al*. 1991) is employed in this study. The cross section of beam and column elements were discretized into small fibers in which each fiber had a prescribed uniaxial stress-strain relationship and fiber sections are integrated along the member using the Gauss-Labotto integration scheme. Each control section consists of confined concrete fibers, unconfined concrete fibers and reinforcing steel bar fibers.

There were no slabs modeled in the 3-D frame structure so effective flange width has to be evaluated to consider the contribution of slabs to the behavior of the frame structure as real situation. Therefore, *L* and *T*-beams were modeled in this study with the effective flange width contributing to both flexural compressive strength and stiffness (Paulay and Priestley 1992). The effective flange width was taken into account by 8 times of slab thickness for *T*-beams and by 3 times for *L*-beams in the analysis.

In order to avoid conflicts of longitudinal bars located in upper and lower precast columns, left side and right side precast beams, the different covers of beam and column elements were considered and designed. In addition, all beam-column joints were assumed to be completely rigid, with the physical size of the joint being represented by rigid end zones in the beams and columns.

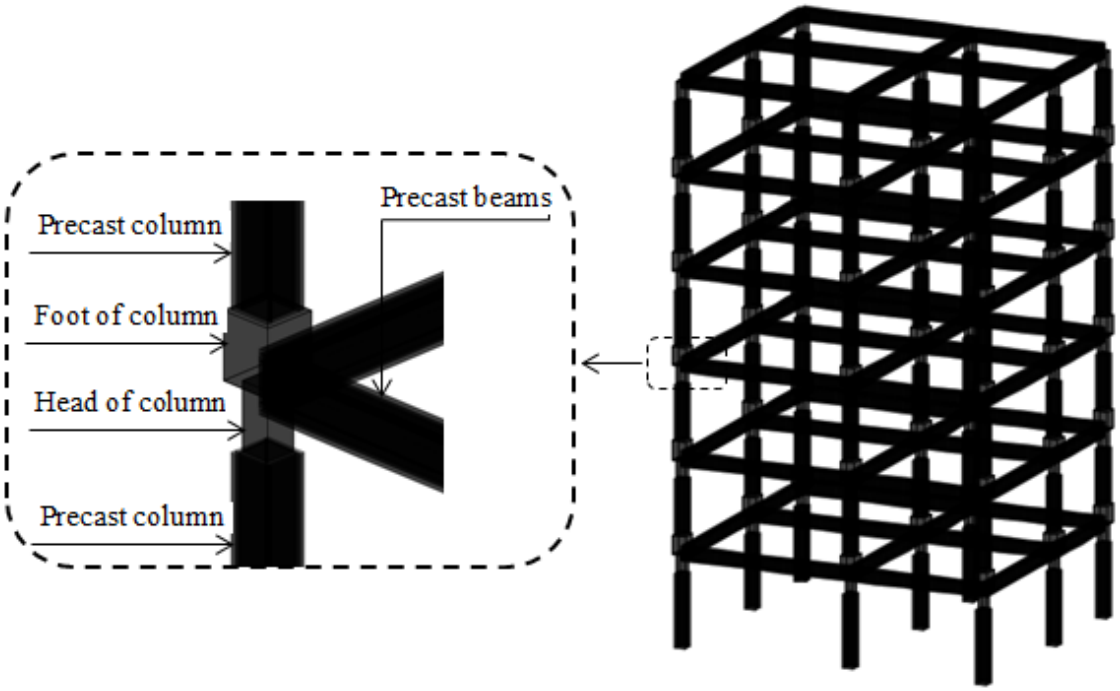

(a) Beam-column joint (b) Overall precast structure modeled

Fig. 6 Simulated model

Thus, the head sections of columns were modeled in order to reflect the interface behavior between precast columns and joint core of CIP joints. Head cross sections of column were reduced 30% compared with the middle sections of columns. In addition, foot cross sections of columns were increase 20% in order to take the contribution of monolithic structural parts including foot of column, beam and slab, to stiffness of joints as shown in Fig. 6(a). The length of such elements is equal to the depth of beam which represents for rigid end zones of columns framing into a joint. The overall precast structure was modeled in Fig. 6(b).

The flexibility-based elements employed in modeling are derived from exact force interpolation functions and therefore not encounter a discretization error, as generally found in the stiffness-based elements (Neuenhofer and Filippou 1997). The main advantage of flexibility formulations with respect to a displacement formulation is the use of interpolation functions to obtain the internal forces starting from the forces at the element nodes. Such functions are actually exact for frame elements and their determination from equilibrium is straightforward (Valipour and Foster 2007).

4.4 Loading

The applied load for this numerical model consisted of dead load and seismic load. The dead load including self-weight of frame structure and distributed span load which was simulated from the uniform load on slabs and self-weight of slabs. The load intensity was uniform and applied to full beam element lengths.

Table 5 Simulated and tested natural frequency

After test phase	PGA (g)								
	Initial	0.066	0.13	0.185	0.264	0.37	0.415	0.55	0.75
					X direction- Simulated result				
1st Frequency (Hz)	4.110	3.915	3.439	2.953	2.950	2.817	2.418	2.408	2.323
2nd Frequency (Hz)	12.578	12.285	11.576	10.888	10.852	10.414	8.687	8.644	8.305
					X direction- Tested result				
1st Frequency (Hz)	4.125	3.750	3.125	2.875	2.500	2.125	1.750	1.625	1.000
2nd Frequency (Hz)	13.625	12.625	11.125	10.750	9.875	9.125	8.000	7.250	6.500
					Y direction- Simulated result				
1st Frequency (Hz)	4.213	4.213	4.212	4.199	4.197	4.168	4.095	4.091	4.051
2nd Frequency (Hz)	12.879	12.823	12.878	12.847	12.842	12.763	12.749	12.493	12.313
					Y direction- Tested result				
1st Frequency (Hz)	4.245	4.125	3.750	3.375	3.250	2.625	2.375	2.125	1.875
2nd Frequency (Hz)	13.750	13.250	11.875	11.500	11.250	10.375	9.250	8.750	7.750

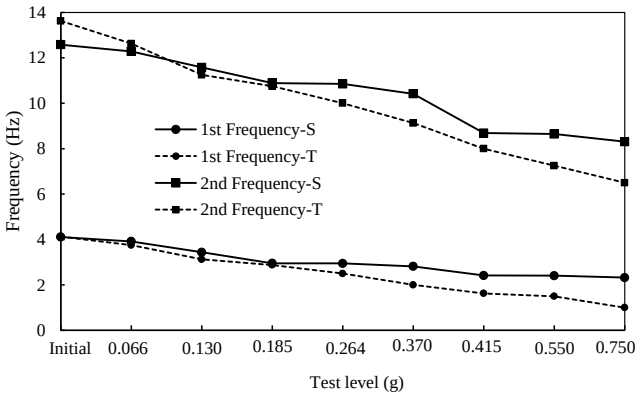

(a) Simulated and tested natural frequencies in *X*-direction

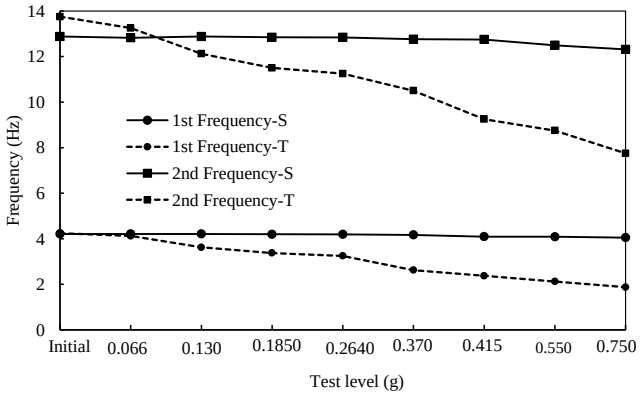

(b) Simulated and tested natural frequencies in *Y*-direction

Fig. 7 Simulated and tested natural frequency
(Note: the symbol "*T*" refers to tested results; "*S*" refers to simulated results)

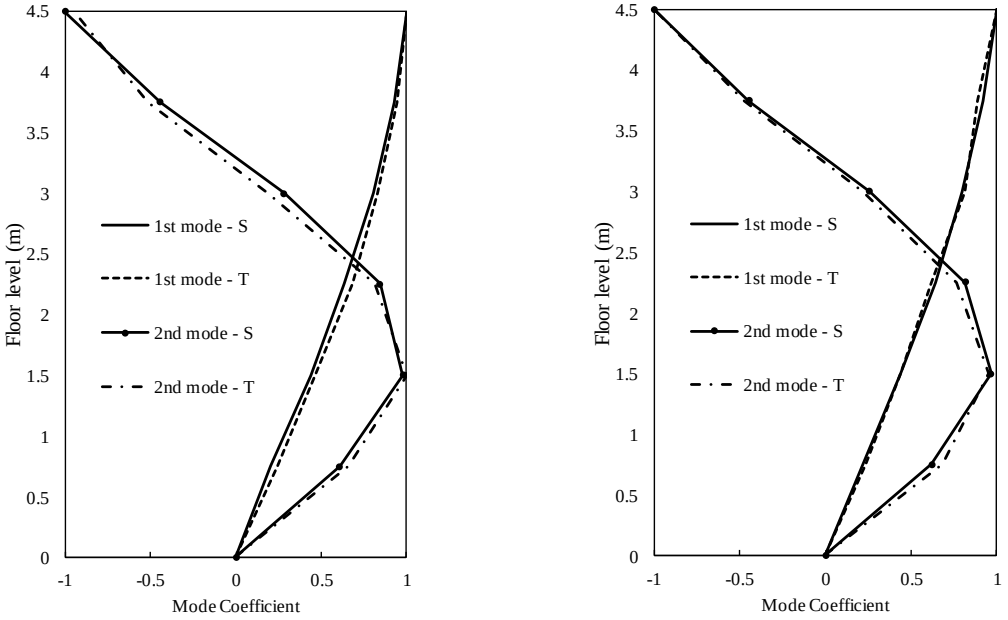

(a) Mode shapes in *X*-direction (b) Mode shapes in *Y*-direction

Fig. 8 Simulated and tested mode shapes
(Note: the symbol "*T*" refers to tested results; "*S*" refers to simulated results)

The ground motions obtained from the shaking table test were input to the models. The seismic waves WCW, ELW and SHW were inputted in sequence with gradually increasing amplitude as the shaking table test, which are PGA of 0.066 g, 0.130 g, 0.185 g, 0.264 g, 0.370 g, 0.415 g, 0.550 g, and 0.750 g. The sequence of inputs imposed to simulated model in series is presented in Table 1.

5. Simulated results and validation

5.1 Dynamic characteristics

Table 5 compares the natural frequencies of the first two vibration modes in *X* and *Y* directions obtained from the simulations and the shaking table tests. It can be seen that the simulated frequencies agree well with the test results, especially the initial frequencies in *X* direction of the first mode. The comparisons between the tested and simulated natural frequencies are displayed in Fig. 7.

As shown in Fig. 7, in the *X*-direction, both the tested natural frequency and the simulated results descend continuously during a series of excitations with gradually increasing acceleration amplitudes. However, after 0.415 g test phase, the tested natural frequency still tend to decline, while the simulated natural frequencies remains relatively steadily. This may be due to the severe damage of the model when suffered from such a high PGA whereas the simulation cannot take this damage into account very well (Filippou *et al*. 1992). In addition, the interaction between shaking table and structure also causes a reduction in the structural frequency (Rinawi and Clough 1991).

In the *Y*-direction, the tested natural frequency tend to decline, while the simulated natural frequencies remains steadily. It is likely that the earthquake loads were only input in the *X*-direction so the damage could not be calculated in the *Y*-direction in modeling but it was well considered in the shaking table test with white-noise scanning in both *X*- and *Y*- directions

The structural vibration modes in both *X* and *Y*- directions obtained from numerical analysis compared with results from shaking table test at initially are shown in Fig. 8 (a, b), respectively. The results show that numerical vibration modes are quite similar to the experimental vibration modes, and most relative errors of mode coefficients of the first two vibration modes are within 10% as presented in Table 6. Both tested and simulated first-order vibration modes in Fig. 8 show a typical shear type feature, as usually occurs in a normal frame structure and are all uniformly distributed along the height.

Table 6 Simulated and tested mode coefficient

Floor level (m)	*X*-Direction						*Y*-Direction					
	Mode 1			Mode 2			Mode 1			Mode 2		
	T	*S*	*V* (%)	*T*	*S*	*V* (%)	*T*	*S*	*V* (%)	*T*	*S*	*V* (%)
0.75	0.25	0.21	-16.0	0.66	0.61	-7.3	0.24	0.22	-9.6	0.69	0.62	-9.2
1.50	0.47	0.44	-6.7	1.00	0.98	-2.0	0.44	0.44	1.1	0.95	0.97	1.3
2.25	0.68	0.64	-6.6	0.81	0.85	4.1	0.62	0.64	3.0	0.77	0.82	7.0
3.00	0.83	0.80	-3.0	0.19	0.28	49.0	0.81	0.80	-1.2	0.22	0.26	20.5
3.75	0.94	0.93	-1.9	-0.52	-0.44	-14.1	0.89	0.92	4.1	-0.48	-0.45	-5.8
4.50	1.00	1.00	0.0	-0.95	-1.00	5.3	1.00	1.00	0.0	-1.00	-1.00	0.0

Table 7 Simulated and tested acceleration amplification factors

Earthquake level (g)		Floor level (m)																	
		0.75			1.50			2.25			3.00			3.75			4.50		
		T	*S*	*V* (%)	*T*	*S*	*V* (%)	*T*	*S*	*V* (%)	*T*	*S*	*V* (%)	*T*	*S*	*V* (%)	*T*	*S*	*V* (%)
0.07	WCW	1.98	1.14	-42	2.25	1.89	-16	2.47	2.22	-10	2.47	2.75	12	2.58	3.17	23	3.48	3.66	5
	ELW	1.93	1.11	-43	2.39	1.75	-27	2.84	2.27	-20	3.17	2.74	-14	3.71	3.17	-14	4.59	3.64	-21
	SHW	1.72	1.43	-17	2.73	2.34	-14	2.95	2.97	1	3.28	3.41	4	3.71	3.73	0	4.17	4.59	10
0.13	WCW	1.63	1.05	-35	1.92	1.94	1	2.16	2.09	-3	2.15	2.15	0	2.50	2.22	-11	2.68	2.59	-3
	ELW	1.77	1.38	-22	2.42	1.98	-18	2.77	2.01	-28	2.90	1.90	-34	3.11	2.31	-26	3.59	2.81	-22
	SHW	1.65	1.82	10	2.22	2.10	-6	2.74	2.83	3	3.07	3.10	1	3.46	2.96	-14	4.19	2.93	-30
0.19	WCW	1.08	1.05	-3	1.53	1.31	-14	1.42	1.26	-11	1.42	1.47	3	1.62	1.63	1	1.91	1.77	-7
	ELW	1.32	1.72	31	1.78	2.13	19	1.79	1.90	6	1.71	1.74	2	1.93	1.73	-10	2.07	2.00	-3
	SHW	1.83	1.55	-15	2.59	2.26	-13	3.16	2.49	-21	2.82	2.80	-1	3.03	2.66	-12	3.40	3.05	-10
0.26	WCW	1.24	0.98	-21	1.63	1.29	-21	1.62	1.32	-19	1.47	1.37	-7	1.71	1.57	-8	2.19	1.71	-22
	ELW	1.13	1.60	41	1.64	2.14	31	1.55	1.91	24	1.51	1.45	-3	1.68	1.73	3	2.21	2.04	-8
	SHW	1.54	1.17	-24	2.01	1.59	-21	1.97	2.12	8	2.02	2.25	12	2.05	2.39	16	2.58	2.56	-1
0.37	WCW	1.36	1.07	-22	1.48	1.48	0	1.80	1.32	-26	1.59	1.26	-21	1.61	1.42	-12	2.13	1.60	-25
	ELW	1.09	1.25	14	1.44	1.79	25	1.31	1.53	17	1.06	1.47	38	1.16	1.57	35	1.52	1.65	9
	SHW	1.59	1.36	-14	2.01	1.62	-19	2.04	2.08	2	2.20	2.20	0	2.40	2.44	2	2.53	2.60	3

Table 7 Continued

	WCW	1.20	1.16	-4	1.40	1.60	14	0.99	1.60	62	0.92	1.22	32	1.05	1.09	3	1.53	1.15	-25
0.42	ELW	1.08	1.10	1	0.88	1.37	55	0.86	1.50	75	0.77	1.47	91	0.94	1.63	73	1.10	1.67	52
	SHW	1.30	1.85	42	1.54	2.26	46	1.60	2.24	40	1.64	2.15	31	1.79	2.47	38	2.46	2.75	12
	WCW	1.05	1.12	6	1.38	1.26	-9	0.97	1.37	42	0.90	1.22	35	1.08	1.07	-1	1.53	1.01	-34
0.55	ELW	1.11	0.99	-11	0.88	1.30	47	0.79	1.39	76	0.79	1.33	67	0.87	1.59	83	1.13	1.70	50
	SHW	1.04	1.90	83	1.21	2.12	75	1.03	1.70	65	1.12	1.77	58	1.26	1.75	38	1.62	2.48	53
	WCW	0.78	1.40	79	0.96	1.12	17	0.77	1.47	90	0.73	1.62	123	0.82	1.39	69	0.97	1.28	31
0.75	ELW	1.03	0.70	-32	1.09	1.17	7	0.72	0.93	29	0.85	1.09	28	0.92	1.27	39	0.85	1.49	76
	SHW	1.02	1.21	18	1.08	1.88	74	0.83	1.60	93	1.00	1.25	26	0.96	1.27	32	1.13	1.41	25

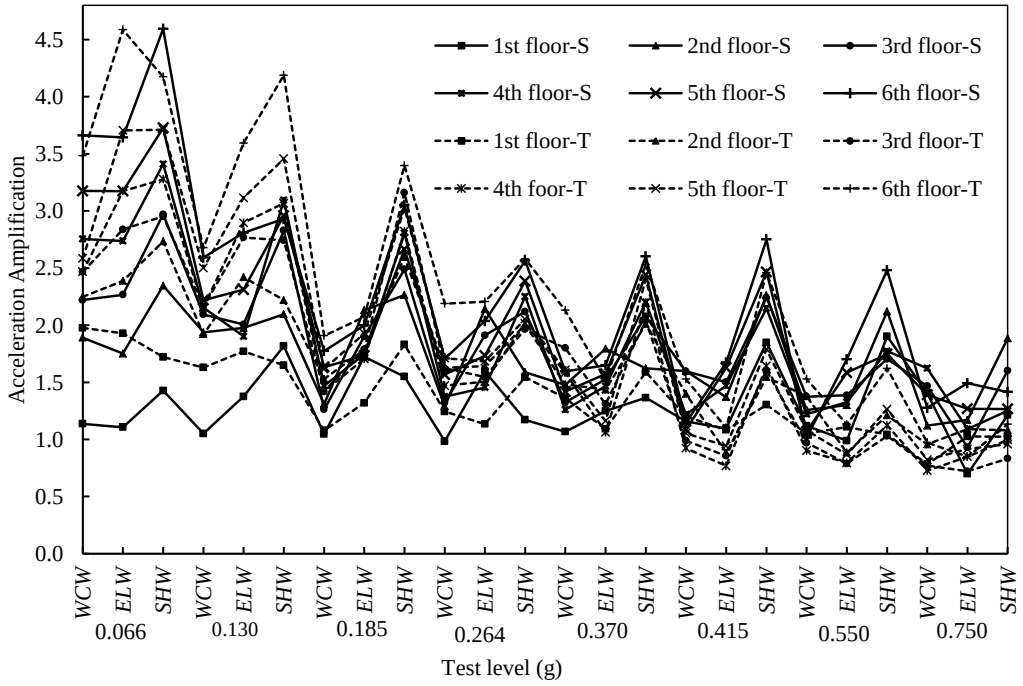

Fig. 9 Simulated and tested acceleration amplification factors vs. input motions

5.2 Acceleration amplification

The acceleration amplification factors are shown in Table 7 and illustrated in Fig. 9. As seen in Fig. 9, the distribution forms of the acceleration amplification factors for both the numerical model and the test model are in general similar. Acceleration amplification factor increases gradually along the height under the same earthquake level, especially in the early test stages when the PGAs are low, and decreases gradually with the increasing PGAs. This trend, however, is not strictly followed in later stages with higher PGA, probably caused by the complicated higher vibration modes due to the accumulation of nonlinear damage. As presented in Table 7, it can be found that before the structure stepped into the severe damage stage (from 0.415g test phase) most relative errors of acceleration amplifying factors are within 25%. Thereafter, most of the relative errors

increase up to over 50% as PGAs of input motions increase. The best agreement is conducted by SHW and followed by WCW and ELW.

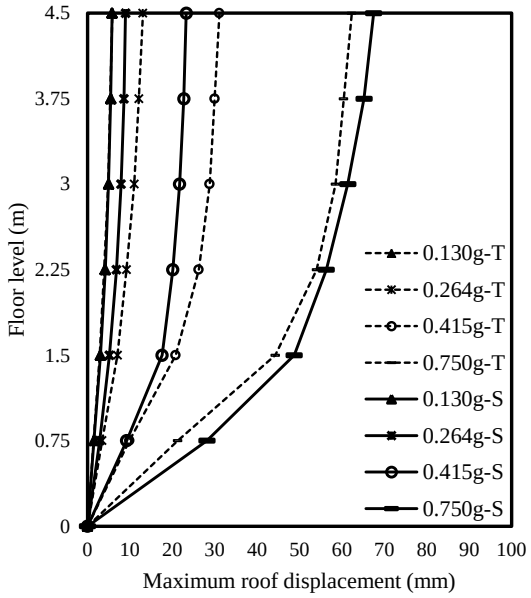

(a) Simulated and tested maximum displacement under WCW

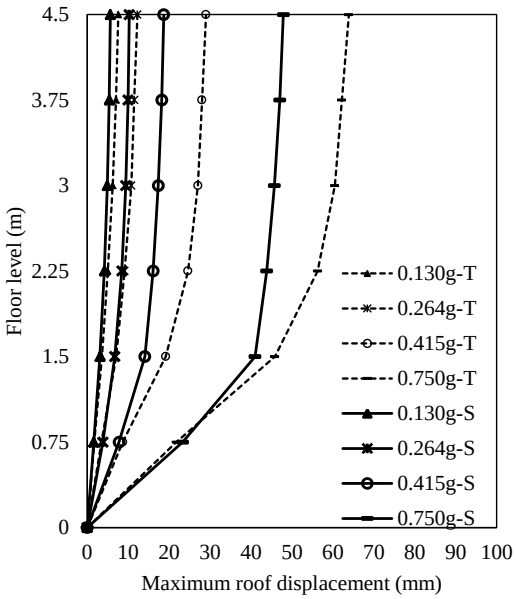

(b) Simulated and tested maximum displacement under ELW

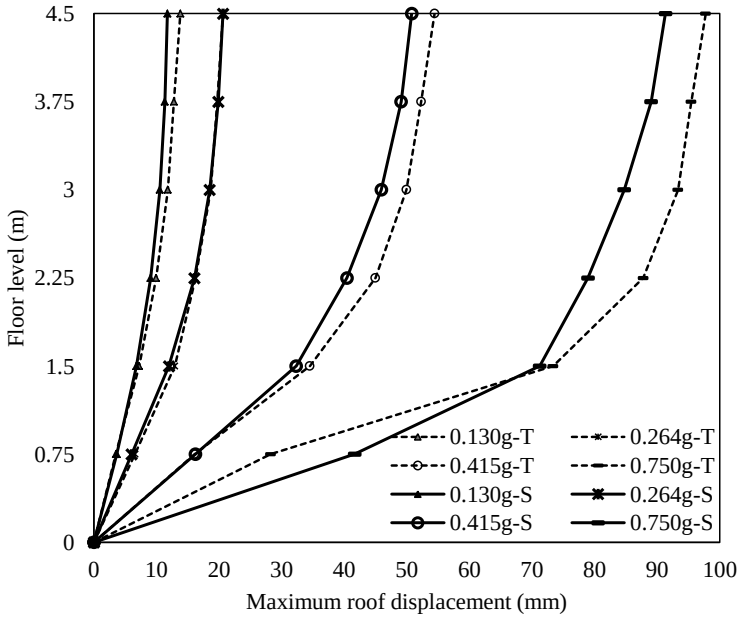

(c) Simulated and tested maximum displacement under SHW

Fig. 10 Simulated and tested maximum displacement of precast RAC model
(Note: the symbol "*T*" refers to tested results; "*S*" refers to simulated results)

Table 8 Simulated and tested maximum displacements

Earthquake level (g)		Floor level (m)																	
		0.75			1.50			2.25			3.00			3.75			4.50		
		T	*S*	*V* (%)	*T*	*S*	*V* (%)	*T*	*S*	*V* (%)	*T*	*S*	*V* (%)	*T*	*S*	*V* (%)	*T*	*S*	*V* (%)
0.066	WCW	0.8	0.7	-17	1.3	1.4	7	1.8	2.1	14	2.2	2.7	21	2.5	3.1	21	2.7	3.3	21
	ELW	0.8	0.6	-19	1.4	1.4	-5	2.0	2.0	1	2.3	2.5	5	2.7	2.9	7	3.0	3.1	3
	SHW	1.0	0.9	-8	1.9	1.9	0	2.7	2.7	2	3.4	3.4	0	3.8	3.9	1	4.2	4.1	-1
0.13	WCW	1.5	1.5	4	2.9	3.0	5	3.9	4.2	7	4.9	5.0	2	5.3	5.5	3	5.8	5.8	-1
	ELW	1.7	1.6	-7	3.6	3.1	-14	5.0	4.2	-17	6.2	4.9	-21	7.0	5.4	-23	7.6	5.6	-26
	SHW	3.5	3.7	5	7.2	6.8	-6	9.9	9.1	-9	11.8	10.5	-11	12.8	11.3	-11	13.8	11.8	-15
0.185	WCW	2.3	2.4	2	4.6	4.3	-6	6.2	5.8	-8	7.5	6.8	-10	8.3	7.3	-12	8.9	7.6	-14
	ELW	2.7	2.8	5	5.2	4.9	-6	6.9	6.3	-9	8.3	7.1	-15	8.9	7.5	-15	9.7	7.8	-20
	SHW	4.7	4.4	-8	8.8	7.9	-10	11.3	10.3	-9	13.4	11.7	-12	15.1	12.6	-17	15.7	12.9	-18
0.264	WCW	3.4	2.9	-16	7.1	5.2	-27	9.2	6.8	-26	11.0	7.9	-28	12.1	8.6	-29	13.1	9.0	-31
	ELW	3.5	3.8	10	7.1	6.7	-5	9.1	8.4	-7	10.8	9.4	-13	11.5	10.0	-13	12.3	10.3	-16
	SHW	6.6	6.0	-8	12.9	12.0	-7	16.2	16.1	-1	18.7	18.5	-1	19.7	19.9	1	20.6	20.6	0
0.37	WCW	7.4	5.6	-24	15.3	11.2	-27	19.6	14.9	-24	22.0	16.7	-24	23.7	17.5	-26	24.5	17.9	-27
	ELW	3.8	4.4	14	8.0	8.5	6	10.1	11.3	12	11.6	12.7	9	12.2	13.4	10	12.8	13.8	7
	SHW	11.6	6.2	-47	23.3	12.6	-46	29.8	17.2	-42	34.1	19.9	-42	36.4	21.7	-40	37.5	22.8	-39
0.415	WCW	9.9	9.2	-7	20.8	17.6	-15	26.2	20.1	-23	28.8	21.7	-25	30.0	22.7	-24	31.1	23.3	-25
	ELW	8.7	7.8	-11	19.2	14.1	-27	24.6	16.1	-35	27.0	17.4	-36	28.0	18.2	-35	29.0	18.7	-36
	SHW	16.1	16.2	1	34.5	32.3	-6	45.0	40.4	-10	50.0	45.9	-8	52.3	49.1	-6	54.5	50.8	-7
0.55	WCW	14.1	13.3	-6	29.1	24.9	-15	36.4	29.2	-20	39.7	31.9	-20	41.3	33.6	-19	42.7	34.5	-19
	ELW	11.7	11.1	-5	25.3	20.9	-17	32.5	24.2	-26	35.6	26.3	-26	36.9	27.6	-25	38.2	28.3	-26
	SHW	19.9	28.8	45	40.9	49.8	22	51.3	57.1	11	55.6	62.2	12	57.9	65.9	14	59.7	68.6	15
0.75	WCW	21.3	28.2	32	44.3	48.8	10	54.0	56.3	4	58.5	61.4	5	60.4	65.2	8	62.3	67.5	8
	ELW	21.8	23.3	7	45.8	41.0	-11	56.3	43.8	-22	60.5	45.7	-24	62.2	47.0	-24	63.9	47.9	-25
	SHW	28.3	41.7	47	73.4	71.2	-3	87.8	79.0	-10	93.4	84.8	-9	95.5	89.0	-7	97.8	91.3	-7

5.3 Displacement

The maximum story displacements from numerical analysis and test results are illustrated in Fig. 10. Overall, the simulated and tested relations are shown a very good correlation. Particularly, before the structure stepped into the severe damage stage (from 0.415 g test phase) most relative errors of acceleration amplifying factors are within 15% as shown in Table 8. Thereafter, the difference between the simulated and tested results increases as the input acceleration amplitudes increase gradually and most of the relative errors within 25% as presented in Table 8. The best agreement is conducted by SHW and followed by WCW and ELW. The simulated maximum floor displacements almost reproduce the tested values and the numerical model captures the primary trend of story displacement distribution.

Both simulated and tested results indicate that the structural displacement responses of the

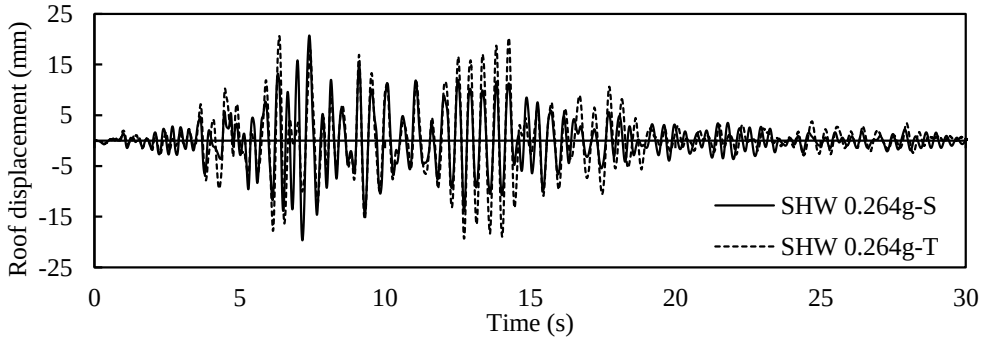

(a) Test phase SHW with PGA of 0.264 g

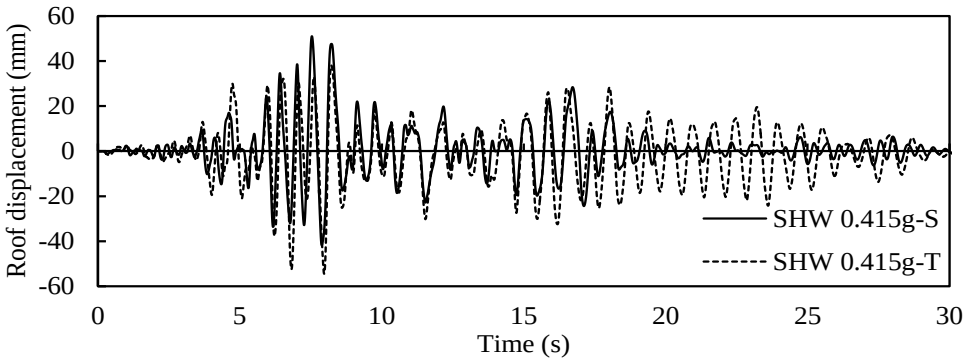

(b) Test phase SHW with PGA of 0.415 g

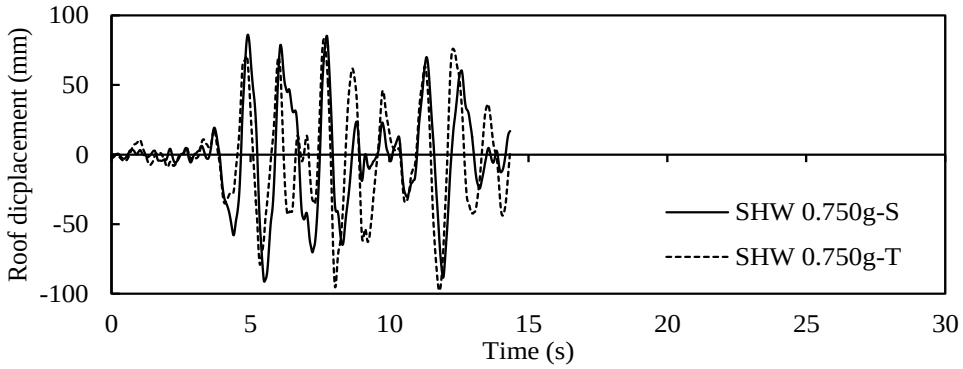

(c) Test phase SHW with PGA of 0.750 g

Fig. 11 Comparisons of simulated and tested roof displacement time histories
(Note: the symbol "*T*" refers to tested results; "*S*" refers to simulated results)

RAC frame model behaved intensely with gradually increasing acceleration amplitudes. Both of the results demonstrate that different earthquake waves slightly influenced the shape of the structural displacement response while they obviously influenced the amplitude of the structural displacement. Fig. 10 shows the story displacements under SHWs are the greatest, followed by the WCW and the ELW, which is consistent with the tested results.

The comparisons of simulated and tested roof displacement time-histories as shown in Fig. 11 verify the accuracy of the nonlinear seismic analysis. As shown in Fig. 11, the simulated model

Table 9 Simulated and tested maximum inter-story drift

Earthquake level		Floor level (m)																	
		0.75			1.5			2.25			3			3.75			4.5		
		T	*S*	*V* (%)	*T*	*S*	*V* (%)	*T*	*S*	*V* (%)	*T*	*S*	*V* (%)	*T*	*S*	*V* (%)	*T*	*S*	*V* (%)
0.066	WCW	0.79	0.65	-17	0.67	0.77	15	0.56	0.69	23	0.53	0.56	5	0.37	0.42	14	0.36	0.27	-26
	ELW	0.78	0.64	-18	0.65	0.71	10	0.54	0.62	14	0.54	0.52	-3	0.41	0.41	-1	0.38	0.26	-32
	SHW	0.99	0.90	-9	0.92	1.00	9	0.81	0.86	6	0.71	0.69	-3	0.47	0.48	3	0.46	0.29	-36
0.130	WCW	1.48	1.54	4	1.48	1.50	2	1.06	1.16	10	0.97	0.90	-8	0.55	0.60	10	0.60	0.34	-43
	ELW	1.71	1.59	-7	1.87	1.50	-20	1.47	1.13	-23	1.29	0.86	-33	0.80	0.66	-18	0.65	0.42	-36
	SHW	3.51	3.67	5	3.76	3.17	-16	2.69	2.27	-16	2.03	1.50	-26	1.22	0.87	-29	1.02	0.49	-52
0.185	WCW	2.31	2.35	2	2.51	2.02	-19	1.66	1.47	-11	1.42	1.00	-30	1.03	0.66	-36	0.79	0.38	-52
	ELW	2.67	2.81	5	2.71	2.14	-21	1.83	1.47	-20	1.54	1.05	-32	0.88	0.75	-15	0.83	0.43	-48
	SHW	4.74	4.35	-8	4.27	3.59	-16	3.13	2.40	-23	2.35	1.58	-33	1.86	0.95	-49	0.92	0.52	-44
0.264	WCW	3.45	2.91	-16	3.63	2.34	-36	2.50	1.69	-32	2.01	1.17	-42	1.17	0.73	-38	0.94	0.41	-57
	ELW	3.47	3.83	10	3.61	2.90	-20	2.31	1.96	-15	1.89	1.32	-30	1.12	0.88	-21	0.93	0.51	-45
	SHW	6.57	6.03	-8	6.38	5.98	-6	4.23	4.75	12	2.71	3.10	14	1.78	1.52	-15	1.20	0.76	-37
0.370	WCW	7.43	5.62	-24	8.02	5.61	-30	4.39	3.67	-16	2.83	2.28	-20	2.00	1.26	-37	1.17	0.70	-40
	ELW	3.81	4.36	14	4.37	4.18	-4	2.58	2.82	9	1.68	2.04	21	0.90	1.13	25	0.77	0.58	-25
	SHW	11.58	6.16	-47	11.89	6.52	-45	6.82	4.85	-29	4.44	3.34	-25	2.38	1.93	-19	1.40	1.02	-27
0.415	WCW	9.88	9.22	-7	11.00	8.41	-24	6.57	2.96	-55	3.55	2.61	-27	1.82	1.77	-3	1.40	0.70	-50
	ELW	8.68	7.76	-11	10.50	6.50	-38	6.07	3.16	-48	3.27	3.01	-8	1.61	1.94	20	1.16	0.88	-24
	SHW	16.12	16.23	1	18.54	16.13	-13	10.98	9.69	-12	5.21	7.62	46	2.67	4.89	83	2.23	2.45	10
0.550	WCW	14.07	13.28	-6	15.18	11.64	-23	8.59	5.33	-38	4.51	3.92	-13	2.31	2.52	9	1.68	1.10	-34
	ELW	11.67	11.07	-5	13.66	9.86	-28	7.47	3.85	-48	4.18	3.53	-16	2.13	2.26	6	1.54	1.00	-35
	SHW	19.88	28.78	45	21.25	21.26	0	10.67	9.46	-11	5.81	7.31	26	2.97	5.07	71	2.02	2.83	40
0.750	WCW	21.30	32.08	51	23.30	24.66	6	10.42	8.90	-15	5.26	6.96	32	2.46	4.91	99	2.14	2.71	27
	ELW	21.8	23.31	7	24.08	18.14	-25	12.12	3.86	-68	5.63	3.21	-43	3.03	2.64	-13	2.28	1.24	-46
	SHW	28.25	41.67	47	45.16	30.46	-33	16.40	8.91	-46	8.56	6.59	-23	5.10	4.35	-15	2.92	2.41	-17

captures not only the primary trend of the roof displacement response but also the values of response. As a result, the simulated and tested roof displacement time-histories match very well.

5.4 Story-drift

The maximum inter-story drift obtained from simulated and tested results are listed in Table 9, and the corresponding inter-story drift ratio curves are illustrated in Fig. 12. As shown in Table 9 and Fig. 12, the general variation trend between the simulated value and the tested result is that the relative error increases gradually with progressively enhancing acceleration amplitudes under different earthquake waves. Before the model was in severe damage stage (from 0.415 g test phase), most of the relative error values are less than 25% and thereafter, most of the relative errors are over 40% as shown in Table 9. In the later test phases with PGAs from 0.415 g, the

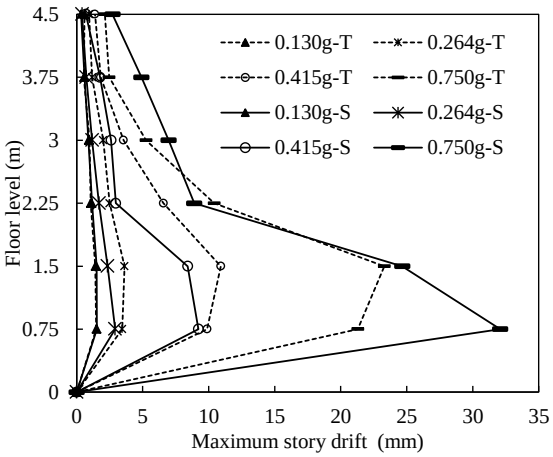

(a) Simulated and tested maximum inter-story drifts under WCW

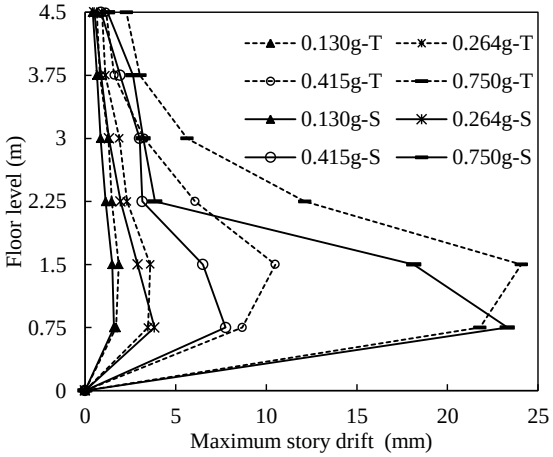

(b) Simulated and tested maximum inter-story drifts under ELW

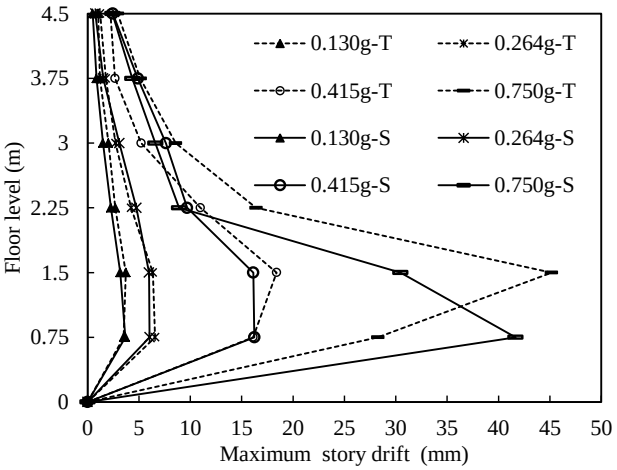

(c) Simulated and tested maximum inter-story drifts under SHW

Fig. 12 Simulated and tested maximum inter-story drift of precast RAC model
(Note: the symbol "*T*" refers to tested results; "*S*" refers to simulated results)

simulated model shown the biggest values of story drifts found at the first floor whereas that of tested results are found at the second floor. In general, the comparison result between the simulated inter-story drift ratio and the experimental under SHW and WCW shows much better agreement than that under ELW.

5.5 Capacity curve

Table 10 presents the values of the comparison of the maximum base shears between simulation and test. The comparison shows that the simulated maximum base shears follow the trend of tested values but smaller than those of test. For instance, most of the relative errors are within 30% until the test phase with PGA of 0.415 g was input. Thereafter, the relative errors

Table 10 Simulated and tested maximum base shear force

Earthquake level (g)		Base shear force (kN)			Earthquake level (g)		Base shear force (kN)		
		T	*S*	*V* (%)			*T*	*S*	*V* (%)
0.066	WCW	13.859	16.660	20.2	0.37	WCW	57.642	42.912	-25.6
	ELW	19.554	16.222	-17.0		ELW	36.749	32.717	-11.0
	SHW	23.066	20.435	-11.4		SHW	64.222	48.082	-25.1
0.13	WCW	30.984	26.865	-13.3	0.415	WCW	40.742	16.995	-58.3
	ELW	35.853	27.353	-23.7		ELW	33.992	15.604	-54.1
	SHW	47.228	37.168	-21.3		SHW	64.324	49.307	-23.3
0.185	WCW	30.916	23.694	-23.4	0.55	WCW	55.688	32.676	-41.3
	ELW	38.250	28.376	-25.8		ELW	41.642	21.590	-48.2
	SHW	52.803	39.007	-26.1		SHW	60.046	49.277	-17.9
0.264	WCW	39.037	25.886	-33.7	0.75	WCW	57.383	45.588	-20.6
	ELW	43.274	34.013	-21.4		ELW	54.156	17.879	-67.0
	SHW	56.314	48.218	-14.4		SHW	57.070	44.541	-22.0

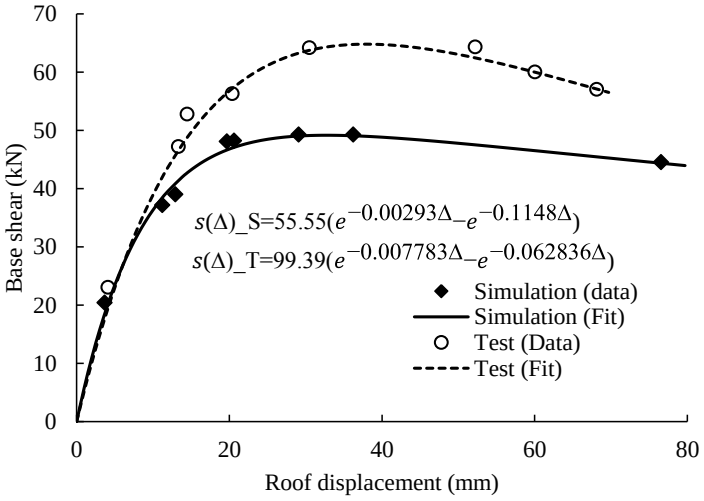

Fig. 13 Simulated and tested capacity curves

increase as the amplitude of PGAs increases, especially in case of WCW and ELW. From the Table 10, it is clearly seen that the best correlation between simulated and tested maximum base shear is under SHW and followed by WCW and ELW.

By tracking the maximum base shear and the corresponding roof displacement, the simulated and tested capacity curve in the form of exponential function is also constructed respectively as in Eq. (1a) and (1b) in order to compare with each other as shown in the Fig. 13.

$$s(\Delta) = 55.55\left(e^{-0.00293\Delta} - e^{-0.1148\Delta}\right) \qquad 0 \le \Delta \le 76.55 \tag{1a}$$

$$s(\Delta) = 99.39\left(e^{-0.007783\Delta} - e^{-0.062836\Delta}\right) \qquad 0 \le \Delta \le 68.11 \tag{1b}$$

Table 11 Feature points on the simulated and tested capacity curves

Feature point parameters		Cracking point (x_C, g_C)	Yielding point (x_Y, g_Y)	Maximum point (x_M, g_M)	Ultimate point (x_U, g_U)
Simulation	Roof displacement (mm)	7.908	11.788	32.766	76.555
	Base shear (kN)	32.987	39.320	49.172	44.370
Test	Roof displacement (mm)	11.845	17.682	37.937	68.114
	Base shear (kN)	43.421	53.892	64.815	55.093
Variation (%)	Roof displacement (mm)	-33	-33	-14	12
	Base shear (kN)	-24	-27	-24	-19

Table 12 Parameters of RAC50 material model for beams

Index		Unconfined concrete					Unconfined concrete				
		f_c' (MPa)	ε_o' (10^{-3})	$0.2f_c'$ (MPa)	ε_{20}' (10^{-3})	E_c (GPa)	Kf_c' (MPa)	ε_o' (10^{-3})	$0.2Kf_c'$ (MPa)	ε_{20}' (10^{-3})	E_c (GPa)
		Precast RAC					Cast-in-place RAC				
Story	1F	42.29	2.20	8.46	3.27	29.76	39.46	2.20	7.89	3.32	29.11
	2F	33.79	2.20	6.76	3.45	27.64	48.32	2.20	9.66	3.16	30.94
	3F	36.39	2.20	7.28	3.39	28.36	41.63	2.20	8.33	3.28	29.62
	4F	34.18	2.20	6.84	3.44	27.74	42.39	2.20	8.48	3.26	29.78
	5F	31.15	2.20	6.23	3.53	26.82	37.80	2.20	7.56	3.36	28.72
	6F	41.57	2.20	8.31	3.28	29.60	36.53	2.20	7.31	3.39	28.39

Table 13 Parameters of RAC50 material model for columns

Index		Unconfined concrete Elastic modulus					Confined concrete Elastic modulus				
		f_c' (MPa)	ε_o' (10^{-3})	$0.2f_c'$ (MPa)	ε_{20}' (10^{-3})	E_c (GPa)	Kf_c' (MPa)	ε_o' (10^{-3})	$0.2Kf_c'$ (MPa)	ε_{20}' (10^{-3})	E_c (GPa)
		Precast RAC					Cast-in-place RAC				
Story	1F	36.19	2.20	7.24	4.63	28.30	40.82	2.48	8.16	53.05	28.30
	2F	34.21	2.20	6.84	4.84	27.76	38.60	2.48	7.72	53.20	27.76
	3F	37.71	2.20	7.54	4.50	28.69	42.52	2.48	8.50	52.95	28.69
	4F	37.55	2.20	7.51	4.51	28.66	42.34	2.48	8.47	52.96	28.66
	5F	36.80	2.20	7.36	4.58	28.46	41.50	2.48	8.30	53.01	28.46
	6F	36.03	2.20	7.21	4.65	28.26	40.64	2.48	8.13	53.06	28.26

where, $s(\Delta)$ is the base shear (kN) and Δ is the roof displacement (mm).

The illustration from Fig. 13 reveals that the simulated capacity curve coincides with the tested capacity curves when the model behaves in the linear stage. After the cracks appeared, which is determined by cracking point as presented in Table 11, the simulated structure passed the yield load and reached the maximum load, which are 27% and 24% smaller than those of test results, respectively. Then, the load capacity and lateral stiffness of the overall structure of the simulated

curve reduces less than those of test results. Although the values of feature points on the simulated curve are lower than those of test around 25%, the simulated capacity curve can reflect both the variation of the load capacity and lateral stiffness of the overall structure.

6. Parametric study

Compressive strength and elastic modulus of RAC are significantly influenced by replacement percentages of RCA. The parametric studies of RAC take the compressive strength and elastic modulus into consideration which represent another grade of RAC by a different replacement ratio of RCA. The tested model and simulated model which was validated above used RCA replacement percentage of 100%, so hereafter called RAC100 model. In the second numerical model simulated, the compressive strength of RAC was increased 30% and elastic modulus was increased 20% in order to investigate influence on the lateral loading capacity of the structures, so herein named such concrete material in the second model as RAC50. The parameters of RAC50 used in modeling of the second model are presented in Tables 12-13.

The initial stiffness of the RAC50 model increases as the results of natural frequencies are shown in Table 14. Consequently, the natural frequencies of the RAC50 model are increased around 9% due to the increase of 20% elastic modulus of RAC. It results in the increase of the base shear when structures subjected to seismic load.

Table 15 presents the comparison of the maximum base shears between simulated RAC100 and RAC50 models. The comparison shows that most of the maximum base shears of RAC50 model are bigger than that of RAC100 model, especially, under the test phases caused by ELW and WCW.

By tracking the maximum base shear with different amplitude of PGAs under three seismic waves and the corresponding roof displacement, the lateral load capacity of RAC50 model is also caused by SHW waves as shown in Table 15. The simulated capacity curve of the RAC50 model in the form of exponential function is also constructed, as presented in the formula of Eq. (2), in order to compare with simulated capacity curve of RAC100 model as shown in the Fig. 14.

$$s(\Delta) = 72.65\left(e^{-0.007114\Delta} - e^{-0.0905\Delta}\right) \qquad 0 \leq \Delta \leq 56.05 \tag{2}$$

where, $s(\Delta)$ is the base shear (kN) and Δ is the roof displacement (mm).

The illustration from Fig. 14 reveals that the trends of the two capacity curves are similar. They behave the same in the elastic stage. After the cracks appeared, which is determined by cracking point as presented in Table 16, the simulated RAC50 model passes the yield load and reaches the maximum load, which are 13% and 10% larger than those of the simulated RAC100 model, respectively. Then, the load capacity of the overall RAC50 structure reduces but still higher than

Table 14 Natural frequencies of model RAC100 and RAC50

Initial	*X*-direction		*Y*-direction	
	1st Frequency (Hz)	2nd Frequency (Hz)	1st Frequency (Hz)	2nd Frequency (Hz)
RAC50 model	4.475	13.691	4.565	13.963
RAC100 model	4.110	12.578	4.210	12.879
Variation (%)	8.9	8.9	8.4	8.4

Table 15 Maximum base shear force of model RAC100 and RAC50

Earthquake level (g)		Base shear force (kN)			Earthquake level (g)		Base shear force (kN)		
		RAC50	RAC100	*V* (%)			RAC50	RAC100	*V* (%)
0.066	WCW	19.01	17.25	10	0.37	WCW	44.82	42.91	4
	ELW	18.01	15.99	13		ELW	37.42	32.99	13
	SHW	27.32	21.65	26		SHW	47.35	48.04	-1
0.13	WCW	23.86	26.84	-11	0.415	WCW	24.69	18.45	34
	ELW	28.37	27.42	3		ELW	17.83	15.76	13
	SHW	35.78	39.68	-10		SHW	53.80	49.31	9
0.185	WCW	34.99	21.21	65	0.55	WCW	48.72	30.42	60
	ELW	34.86	27.14	28		ELW	19.60	21.96	-11
	SHW	44.01	38.84	13		SHW	52.95	49.75	6
0.264	WCW	25.25	22.84	11	0.75	WCW	47.57	46.43	2
	ELW	36.22	34.83	4		ELW	28.31	21.36	33
	SHW	49.63	48.20	3		SHW	48.10	46.01	5

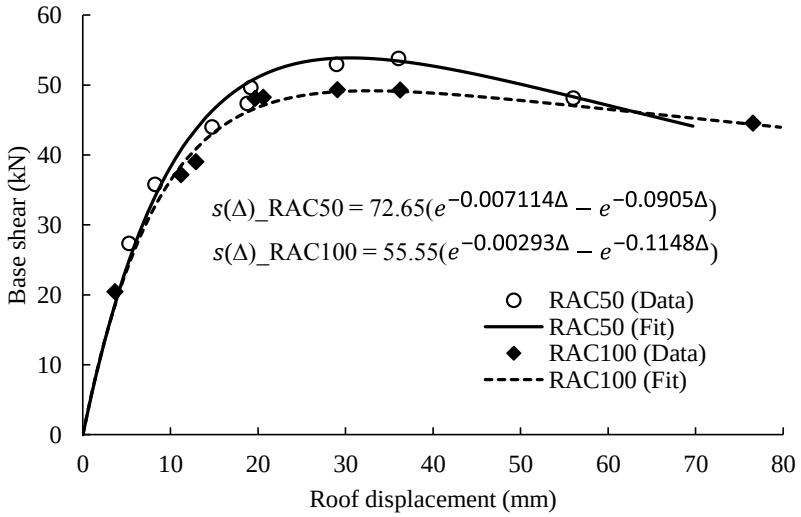

Fig. 14 Capacity curves of two simulated models

Table 16 Feature points on capacity curves of two simulated models

Feature point parameters		Cracking point (x_C, g_C)	Yielding point (x_Y, g_Y)	Maximum point (x_M, g_M)	Ultimate point (x_U, g_U)
RAC50	Roof displacement (mm)	8.898	13.425	30.510	56.049
	Base shear (kN)	35.710	44.464	53.878	48.305
RAC100	Roof displacement (mm)	7.908	11.788	32.766	76.555
	Base shear (kN)	32.987	39.320	49.172	44.370
Variation (%)	Roof displacement (mm)	13	14	-7	-27
	Base shear (kN)	8	13	10	9

those of RAC100 model.

Based on the Table 16, it can be seen that the increase of compressive strength and elastic modulus of RAC result in the increase of the lateral load capacity and reduction of the roof displacement. As a result, the simulated capacity curves of both models can reflect both the variation of the load capacity and lateral stiffness of the overall structure.

7. Conclusions

The significant findings of the present simulation study are given as follows:

(1) The numerical analyses confirm that the flexibility-based beam-column element type, the fiber section model, the confined/unconfined concrete model, the steel hysteretic material model, and the numerical methods used in OpenSees framework are reasonable.

(2) The OpenSees numerical model can reproduce accurately the seismic performance of the RAC frame structure by verification of the test results. Generally, most of the relative error values are less than 25% in the linear range and 40% in the nonlinear range, so the acceptable agreement between the calculated and tested results in terms of the dynamic characteristics, the story displacement, as well as the inter-story drift, shows that the dynamic response can be simulated by the numerical model.

(3) The influence of interface between head columns and CIP joint to stiffness of rigid joints was modeled by reducing cross sections of head columns and validated by test results. The comparison between simulated and tested results shows a good correlation.

(4) Tolerances of construction, inherent errors of instruments, interaction between shake table and structure, higher-mode response, action of interface, joint failure of the tested model, critical damping ratios, constitutive material models employed in simulation are considered the main causes of the difference in simulated dynamic responses compared with tested results.

(5) Both experimental and numerical simulation analysis shown that the precast RAC frame structure, in which precast RAC beams and columns elements were connected by cast-in-place RAC, has enough capacity to resist a severe earthquake load. The good seismic resistance of the model has been convectively proved by the results of the shaking table test and a further report on analysis and evaluation of seismic performance of the precast RAC frame structure will be devoted to enhance the emulation of such kind of precast frame structure. Therefore, the construction process and designing of the model could be considered as a reference for aseismic precast frame structures made of RAC.

Acknowledgements

The authors would like to acknowledge the financial support from the National Natural Science Foundation of China (51325802, 51438007). Especially, the authors would like to acknowledge Prof. Sashi K. Kunnath by his active and significant discussions.

References

Bhikshma, V. and Kishore, R. (2010), "Development of stress-strain curves for recycled aggregate concrete", *Asian J. Civ. Eng.*, **11**(2), 253-261.

Cao, W.L., Yin, H.P. and Zhang, J.W. (2011), "Seismic behavior experiment of recycled concrete frame structures", *J. Beijing University Tech*., **37**(2), 191-198. (in Chinese)

Chinese Standard GB 50011-2010 (2008), *Code for Seismic Design of Buildings*, Chinese Building Press, Beijing, China.

D'Amato, M., Braga, F., Gigliotti, R., Kunnath, S.K. and Laterza, M. (2012), "A numerical general-purpose confinement model for non-linear analysis of R/C members", *Comput. Struct*., **102**, 64-75.

Du, Y.F. and Wang, S.L. (2015), "Shaking table test of high performance RAC frame structure under rare earthquake", *The 3rd International Conference on Mechatronics, Robotics and Automation (ICMRA 2015).*

Fathifazl, G., Razaqpu, A.G. and Isgor, O.B. (2010), "Shear strength of reinforced recycled concrete beams with wtirrups", *Mag. Concr. Res.*, **62**(10), 685-699.

Fathifazl, G., Razaqpur, A.G. and Isgor, O.B. (2009), "Flexural performance of steel-reinforced recycled concrete beams", *ACI Struct. J*., **106**(6), 858-867.

Filippou, F.C., D'Ambrisi, A. and Issa, A. (1992), "Nonlinear static and dynamic analysis of reinforced concrete subassemblages", Report No. UCB/EERC–92/08, Earthq. Eng. R. Center, University of California, Berkeley.

Fonseca, N., Brito, J. and Evangelista, L. (2011), "The influence of curing conditions on the mechanical performance of concrete made with recycled concrete waste", *Cement Concrete Compos.*, **33**(6), 637-643.

Gavali, P.G. and Shah, M.S. (2008), "Earthquake simulations of large scale structures using opensees software on grid and high performance computing in India", *The 14th World Conference on Earthquake Engineering (WCEE)*, Beijing, China.

Kent, D.C. and Park, R. (1971), "Flexural members with confined concrete", *ASCE J. Struct. Div.*, **97**(7), 1969-1990.

Limbachiya, M.C. (2004), "Performance of recycled aggregate concrete", *RILEM International Symposium on Environent-Consciuos Material and Systems for Sustainable Development*, RILEM Publications SARL.

Lo, C.Y. (2008), "Comparison of recycled and natural aggregate properties", *The 3rd ACF International Conference-ACF/VCA*, Ho Chi Minh, November.

Mander, B., Priestley, M.J.N. and Park, R. (1988), "Observed stress-strain behavior of confined concrete", *J. Struct. Eng.*, ASCE, **114**(8), 1827-1849.

Mazzoni, S., Mckenna, F. and Fenves, G.L. (2011), "Open system for earthquake engineering simulation user command language manual", Version 2.3.2. Pacific Earthq. Eng. R. Center, University of California, Berkeley.

Morales, J.D. (2011), "Numerical simulations of steel frames equipped with friction-damped diagonal-bracing devices", The Department of Building, Civil & Environmental Engineering, Concordia University, Montreal, Quebec.

Montya, E. (2000), "Modeling of confined concrete", Department of Civil Engineering, University of Toronto: National Library of Canada.

Neuenhofer, A. and Filippou, F.C. (1997), "Evaluation of nonlinear frame finite element models", *J. Struct. Eng*., ASCE, **123**, 958-966.

Orakcal, K., Massone, L.M. and Wallace, J.M. (2006), "Analytical modeling of reinforced concrete walls for predicting flexural and coupled-shear-flexural responses", Pacific Earthq. Eng. R. Center, College of Engineering University of California, Berkeley.

Parekh, D.N. and Modhera, C.D. (2011), "Characterization of recycled aggregate concrete", *Int. J. Adv. Eng. Tech.*, **2**(4), 321-330.

Quaranta, G., Kunnath, S.K. and Sukumar, N. (2012), "Maximum-entropy meshfree method for nonlinear static analysis of planar reinforced concrete structures", *Eng. Struct.*, **42**, 179-189.

Paulay, T. and Priestley, M.J.N. (1992), *Seismic design of reinforced concrete and masonary buildings*, John Wiley & Sons, Inc., USA.

Rinawi, A.M. and Clough, R.W. (1991), "Shaking table-structure interaction", Report to the national Science Foundation 1991. Report No.UCB/EERC-91/13.

Scott, B.D., Park, R. and Priestley, M.J.N. (1982), "Stress-strain behavior of concrete confined by overlapping hoops at low and high strain rates", *J. Am. Concr. Inst.*, **79**(1), 13-27.

Taucer, F.T., Enrico, S. and Filippou, F.C. (1991), "A fiber beam-column element for seismic response analysis of reinforced concrete structurees", Earthq. Eng. R. Center, College of Eng., Univ. of California, Berkeley.

Valipour, H.R. and Foster, S.J. (2007), "A novel flexibility based beam-column element for nonlinear analysis of reinforced concrete frames", The University of New South Wales.

Xiao, J.Z., Sun, Y.D. and Falkner, H. (2006), "Seismic performance of frame structures with recycled aggregate concrete", *Eng. Struct.*, **28**(1), 1-8.

Xiao, J.Z., Tawana, M.M. and Wang, P.J. (2010), "Test on the seismic performance of frame joints with pre-cast recycled concrete beams and columns", *Proceedings of the 2nd International Conference on Waste Engineering and Management*, Shanghai, China, October.

Xiao, J.Z., Li, W.G., Fan, Y.H. and Huang, X. (2012), "An overview of study on recycled aggregate concrete in China (1996-2011)", *Constr. Build. Mater.*, **31**, 364-383.

Xiao, J.Z., Pham, T.L., Wang, P.J. and Gao, G. (2014a), "Behaviors of semi-precast composite beams made with recycled aggregate concrete", *Struct. Des. Tall Spec. Build.*, **23**(9), 692-712.

Xiao, J.Z., Wang, C.Q., Pham, T.L., Yang, Z.J. and Ding, T. (2014b), "Nonlinear analysis and test validation on seismic performance of a recycled aggregate concrete space frame", *Struct. Des. Tall Spec. Build.*, **23**(18), 1381-1405.

Xiao, J.Z., Pham, T.L. and Ding, T. (2015a), "Shake table test on a precast frame structure with recycled aggregate concrete", *Adv. Struct. Eng*., **18**(9), 1517-1534.

Xiao, J.Z., Sun, C. and Jiang, X.H. (2015b), "Flexural behaviour of recycled aggregate concrete graded slabs", *Struct. Concrete*, **16**, 249-261.

Yassin, M.H.M. (1994), "Nonlinear analysis of prestressed concrete structures under monotonic and cyclic loads", University of California. Berkeley, California.

Zhang, C.Q., Zhou, Y. and Lu, X.L. (2012), "Comparative experimental study on the seismic performance of reinforced totally-recycled concrete frame and smi-recycled concrete frame", *15 WCEE*, Lisbon, September.

CC